Multistage signal-interactive nanoparticles improve tumor targeting through efficient nanoparticle-cell communications

Zhang, Feng; Zhang, Yiran; Kong, Li; Luo, Huanhuan; Zhang, Yuezhou; Mäkilä, Ermei; Salonen, Jarno; Hirvonen, Jouni; Zhu, Yueqi; Chen, Yingsheng; Deng, Lianfu; Zhang, Hongbo; Kros, Alexander ; Cui, Wenguo; Santos, Hélder A.

Multistage signal-interactive nanoparticles improve tumor targeting through efficient nanoparticle-cell communications

Graphical abstract
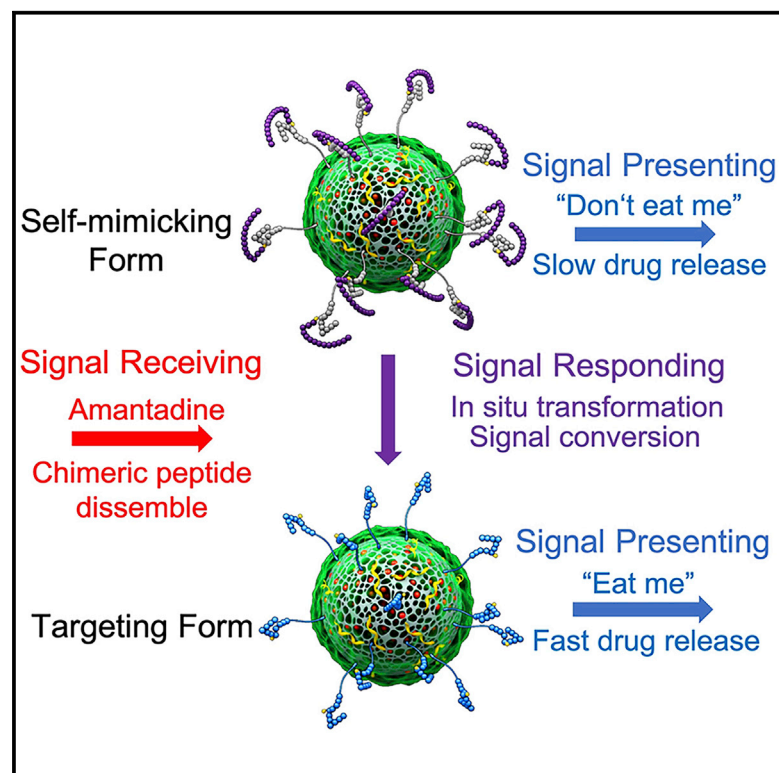
Authors

Feng Zhang, Yiran Zhang, Li Kong, ...,
Alexander Kros, Wenguo Cui,
Hélder A. Santos

Correspondence

hongbo.zhang@abo.fi (H.Z.),
wgcui80@hotmail.com (W.C.),
helder.santos@helsinki.fi (H.A.S.)

In brief

Zhang et al. report a strategy to construct drug delivery NPs with a multistage signal-interactive mechanism to improve the NP-cell communication efficiency. They show that the system can process signals with a "presenting-receiving-responding-presenting" pattern to enhance homeostasis of NPs in the biological environment, resulting in reduced NP clearance by the immune system, enhanced tumor targeting, and enhanced tumor suspension efficacy.

Highlights

- Constructing a signal-interactive NP system improves NP-cell communication efficiency

- Functional chimeric peptide design enables orderly integrating of multiple signal modules

- Signal-interactive NPs reduce liver accumulation and promote tumor targeting

Report

Multistage signal-interactive nanoparticles improve tumor targeting through efficient nanoparticle-cell communications

Feng Zhang,[1,2,10] Yiran Zhang,[2,10] Li Kong,[3,4,10] Huanhuan Luo,[2] Yuezhou Zhang,[5] Ermei Mäkilä,[6] Jarno Salonen,[6] Jouni T. Hirvonen,[1] Yueqi Zhu,[7] Yingsheng Cheng,[7] Lianfu Deng,[2] Hongbo Zhang,[2,8,*] Alexander Kros,[4] Wenguo Cui,[2,*] and Hélder A. Santos[1,9,11,*]

[1]Drug Research Program, Division of Pharmaceutical Chemistry and Technology, Faculty of Pharmacy, University of Helsinki, Helsinki 00014, Finland
[2]Department of Orthopaedics, Shanghai Key Laboratory for Prevention and Treatment of Bone and Joint Diseases, Shanghai Institute of Traumatology and Orthopaedics, Ruijin Hospital, Shanghai Jiao Tong University School of Medicine, 197 Ruijin 2nd Road, Shanghai 200025, P.R. China
[3]Tongji School of Pharmacy, Huazhong University of Science and Technology, Wuhan 430030, P.R. China
[4]Leiden Institute of Chemistry, Leiden University, P.O. Box 9052, 2300 RA Leiden, the Netherlands
[5]Xían Institute of Flexible Electronics & Xían Institute of Biomedical Materials and Engineering, Northwestern Polytechnical University (NPU), 127 West Youyi Road, Xían 710072, P.R. China
[6]Laboratory of Industrial Physics, Department of Physics and Astronomy, University of Turku, 20014 Turku, Finland
[7]Department of Radiology, Shanghai Jiao Tong University Affiliated Sixth People's Hospital, No. 600, Yishan Road, Shanghai 200233, P.R. China
[8]Pharmaceutical Sciences Laboratory, Åbo Akademi University; Turku Bioscience Centre, University of Turku and Åbo Akademi University, Turku 20520, Finland
[9]Helsinki Institute of Life Science (HiLIFE), University of Helsinki, 00014 Helsinki, Finland
[10]These authors contributed equally
[11]Lead contact
*Correspondence: hongbo.zhang@abo.fi (H.Z.), wgcui80@hotmail.com (W.C.), helder.santos@helsinki.fi (H.A.S.)
https://doi.org/10.1016/j.celrep.2021.109131

SUMMARY

Communication between biological components is critical for homeostasis maintenance among the convergence of complicated bio-signals. For therapeutic nanoparticles (NPs), the general lack of effective communication mechanisms with the external cellular environment causes loss of homeostasis, resulting in deprived autonomy, severe macrophage-mediated clearance, and limited tumor accumulation. Here, we develop a multistage signal-interactive system on porous silicon particles through integrating the Self-peptide and Tyr-Ile-Gly-Ser-Arg (YIGSR) peptide into a hierarchical chimeric signaling interface with "don't eat me" and "eat me" signals. This biochemical transceiver can act as both the signal receiver for amantadine to achieve NP transformation and signal conversion as well as the signal source to present different signals sequentially by reversible self-mimicking. Compared with the non-interactive controls, these signal-interactive NPs loaded with AS1411 and tanespimycin (17-AAG) as anticancer drugs improve tumor targeting 2.8-fold and tumor suppression 6.5-fold and showed only 51% accumulation in the liver with restricted hepatic injury.

INTRODUCTION

Communication is universal in biological systems (Perbal, 2003). Biomolecule interactions (such as antigen receptor recognition), signal pathway conduction, and even cell-level behavior that relates to development, homeostasis, and immunity are all communication processes (Sadelain et al., 2013; Bray, 1998; Bloemendal and Kück, 2013). Traditional therapeutic strategies are also achieved by intervening in the communication with biomolecules (mainly proteins, such as receptors, enzymes, and iron channels) via drug molecules (Zhu et al., 2009; Scott et al., 2016). Nevertheless, due to the lack of a direct communication

mechanism on the cellular level, traditional drugs usually lack specific targeting capacity and cause drug-originated systemic toxic effects (Peer et al., 2007). From this perspective, nanoparticles (NPs) emerged as a kind of signal vehicle for conducting communication with cells (Peer et al., 2007; Shi et al., 2017; Yang et al., 2019). Owing to the versatile physical and structural advantages of NPs, combined with the immense developments of modification strategies, it is possible to intervene and regulate cellular behavior or even fate by specifically designed NPs (Tang et al., 2014; Trappmann et al., 2012; Mohammadinejad et al., 2019; Bodelón et al., 2017; Rosenblum et al., 2018). However, when it comes to *in vivo* applications, especially tumor

treatment, the situation is almost reversed. The fate of NPs depends more on the external bio-environment, resulting in severe clearance during blood circulation and limited tumor accumulation (Feliu et al., 2016; Bertrand et al., 2017; Corbo et al., 2016; Wilhelm et al., 2016).

Although the existing biological barriers, especially the mononuclear phagocyte system, are the main reason for the problems of targeting, the limits in understanding and positioning of nanomaterials themselves also restrict the development process (Blanco et al., 2015). Conventionally, under the framework of the "delivery system," NPs are designed to be chosen by the cells, which means the cells have higher priority and initiative than that of NPs during the NP-cell interactions. In this case, the autonomy of NPs will be subordinate to external cell behaviors. Moreover, the inevitable immunogenicity of foreign NPs leads to various immune defenses, which further deprive the autonomy of NPs (Li et al., 2020; Gustafson et al., 2015. Thus, it is difficult to maintain the homeostasis of NPs and to manipulate the fate of NPs *in vivo* (Moghimi and Simberg, 2017; Tsoi et al., 2016). Conservatively, the autonomy of the NPs is hardly to be improved directly by adding functionality or complexity without a NP-cell communication vision (Wilhelm et al., 2016). In the biological environment, signal interactions by communication between individuals are critical for homeostasis maintenance (Mondal et al., 2011). Therefore, NP-cell communication requires that NPs can interact with the cells in a signal-interactive manner, rather than unilaterally receiving signals from cells. However, limited by the current development stage of materials, it is almost unachievable to construct an artificial surface on NPs with a dynamic cell-like communication mechanism (Noireaux et al., 2011; Salehi-Reyhani et al., 2017). Therefore, we hypothesize that an alternative way to achieve this purpose is through modulating in order the signal-presenting process by sequentially integrating different signal models. Based on this understanding, the NPs described here were designed to combine the attributes of "signal receiver," "signal source," and "signal processor," with a "presenting-receiving-responding-presenting" pattern to process signals, termed as a multistage signal-interactive system.

In this study, we chose the Self-peptide and the pentapeptide Tyr-Ile-Gly-Ser-Arg (YIGSR) sequence-contained peptide as the signal-source modules, which can present "don't eat me" and "eat me" signals to cells, respectively (Rodriguez et al., 2013; Sarfati et al., 2011). The Self-peptide contains a functional domain of CD47 glycoprotein, which can act as a "marker of self" to inhibit phagocyte clearance by CD47-SIRPα (signal regulatory protein-α) interaction. It is reported that the Self-peptide-coated particles can also inhibit mouse macrophage uptake through inhibiting cells' contractility-driven uptake by SIRPα signaling (Rodriguez et al., 2013). In addition, the YIGSR peptide can help NPs target to cancer cells that overexpress the relevant receptor β_1-integrine (Sarfati et al., 2011). To integrate these two kinds of signal modules in correct order, we grafted the Self-peptide with β-cyclodextrine (β-CD) to obtain β-CD-conjugated Self-peptide (termed as [β-CD]Self-peptide). The β-CD terminus can form a stable CD-phenol complex with the Tyr in the YIGSR peptide through self-assembly (Chen and Jiang, 2011; Shanmugam et al., 2008; Bouhadiba et al., 2017). The assembled chimeric peptide causes disfunction of YIGSR targeting to β_1-integrine and synchronously

implements self-mimicking, both of which are favorable for enhancing the homeostasis and reducing the immunogenicity of NPs, consequently leading to enhanced tumor accumulation (Graf et al., 1987; Dvir et al., 2010). Moreover, the CD-Tyr complex can also act as a receiving module to exogenous signal of amantadine (Ad), which can disintegrate the CD-Tyr complex by host-guest competition (Figure S1A) (Hu et al., 2014; Smiljanic et al., 2006; Lai et al., 2017). Next, the modified NPs can respond to this Ad signal with *in situ* particle transformation and surface-signal conversion. This process will recover the targeting capacity of YIGSR sequence and facilitate cancer cell uptake of NPs by presenting an "eat me" signal. The whole multistage signal-interactive process is a reversible self-mimicking process, termed here as the [Rev]SeMicNP system (Figures S1B and S1C). After loading tanespimycin (17-AAG) and AS1411 as model drugs, we demonstrate the effectiveness and necessity of the signal-interactive mechanism for communication, which can efficiently manipulate the NP-cell interactions and regulate biodistribution behavior of the NPs by *in vitro* and *in vivo* studies (Figure S1D).

RESULTS

Synthesis and characterizations of the functionalized NPs with chimeric signal peptides

To fabricate the signal modules for communication, the azide polyethylene glycol (N_3-PEG_4) terminus-functionalized (N-Term.)-GGGGYIGSR peptide (YIGSR for short) and N_3-PEG_4 (N-Term.)-Self peptide (with amino acid sequence TCEVTEL-TREGETIIELK) were prepared by standard solid-phase peptide synthesis, and the β-CD terminus was then conjugated to the azido-Self peptide to obtain the [β-CD]Self-peptide by bio-orthogonal strain-promoted alkyne-azide cycloaddition (Figures S2A and S2B). The relevant data of liquid chromatography-mass spectrometry (LC-MS) and matrix-assisted laser desorption/ionization time-of-flight (MALDI-TOF) mass spectrometry are shown in Figures S2C and S2D. Computational mimicking demonstrates the Self-peptide tends to fold from "stretched" state into "bend" conformation (Figure 1A). Figure 1B details the interactions between the Self-peptide and SIRPα on the contact interface and the binding: (1) intra-peptide ionic interaction between Glu 6 and Arg 9 of the peptide helps Arg 9 position to hydrogen bond (3.3 Å) toward the main chain carboxyl oxygen of residue Ala 86 of SIRPα; (2) Thr 88 residue hydroxyl of SIRPα serves as hydrogen bond (2.9 Å) donor to nitrogen on the peptide Glu 6 main chain, which also forms hydrogen bond (3.3 Å) with Glu 110 of SIRPα; and (3) Thr 5 of the peptide also forms weak hydrogen bond (3.6 Å) with side residue of Tyr 90 of SIRPα. The computational docking disclosed the possible binding pose and relative position of the Self-peptide and receptor, showing three different but possible binding complexes (Figure 1C). Figure 1Ca demonstrates the most likely binding pose of experimental peptide based on the docking score and rational analysis. Figures 1Cb and 1Cc enumerate another possible pose of the experimental peptide.

The construction process of [Rev]SeMicNPs is shown in Figure S2E. The size and zeta (ζ)-potential changes of NPs during the fabrication process and the relevant morphological features are shown in Figures 1D and 1E and Figure S3A. Taking
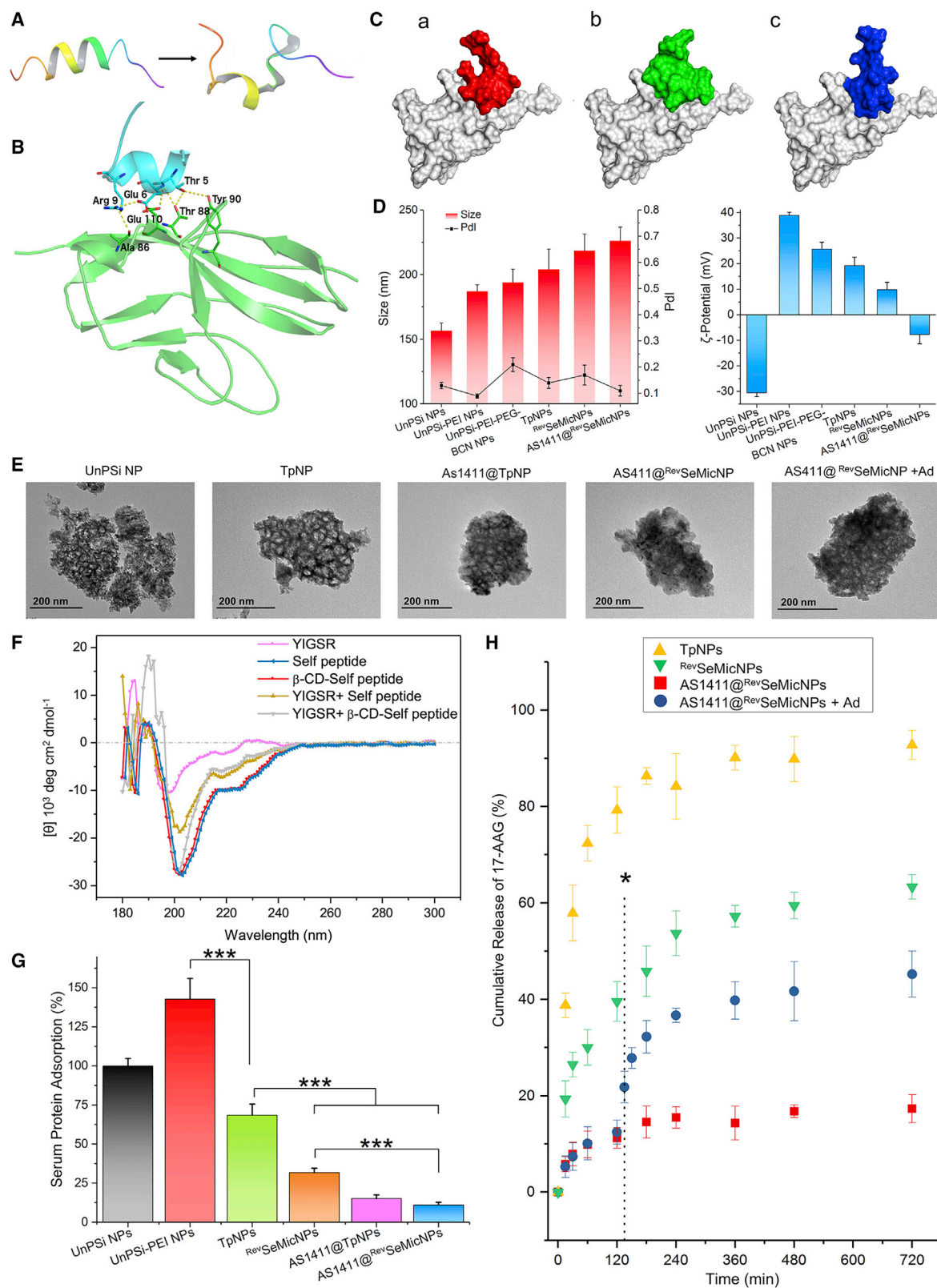
advantage of the chemical-engineering-available surface area and good biocompatibility, undecylenic-acid-modified thermally hydrocarbonized porous silicon NPs (termed as UnPSi NPs) were used as a scaffold to construct the ^{Rev}SeMicNP system (Li et al., 2018; Zhang et al., 2017). First, polyethylenimine (PEI) was bonded onto the surface of PSi NPs to increase modification site and for loading negative oligonucleotide cargos, resulting in a sharp ζ-potential reversion (from −30.6 to 38.9 mV) and 30 nm size increase. Next, the endo-bicyclo[6.1.0]nonyne-PEG$_4$-N-hydroxysuccinimide (BCN-PEG$_4$-NHS) linker was conjugated on the PEI surface for the subsequent azido-YIGSR sequence conjugation onto NPs via azide-alkyne bioorthogonal click (Devaraj, 2018). The obtained YIGSR-coated NPs were still positively charged (19.2 mV), with a hydrodynamic size of 204 nm, termed as TpNPs (short for targeting-peptide-conjugated NPs, which were used as non-interactive NPs for control in the follow-up experiment). Finally, the $^{β-CD}$Self-peptide was grafted by self-assembly with YIGSR to obtain the ^{Rev}SeMicNPs. The relevant size of the NPs was 218 nm and ζ-potential was 9.8 mV. After loading AS411, the size of the NPs increased 8 nm and the ζ-potential changed to −7.8 mV. The Fourier-transform infrared spectroscopy (FTIR) analysis data of the prepared NPs is listed in Figure S3B.

The drug payload test was then performed by high-performance LC (HPLC). The loading ratio of 17-AAG and $^{β-CD}$Self-peptide was 6.9 and 11.5 wt %, respectively. The maximum loading degree of AS1411 was 8.2 wt %, determined using ultraviolet-visible (UV-vis) spectroscopy. However, as the loading amount of AS1411 affected the ζ-potential of NPs (Figure S3C), we chose 5.0 wt % to obtain a slightly negative-charged surface to reduce protein adsorption (Lundqvist et al., 2008).

Circular dichroism measurements were then used to test the interactions between different peptide sequences (Figure 1F). YIGSR showed a predominantly random coil structure, while Self-peptide showed a predominantly α-helical structure, even with β-CD terminus. Moreover, circular dichroism indicated that the presence of β-CD did not affect the configuration of Self-peptide. Furthermore, the inclusive complexes formed between Tyr residue on YIGSR and the β-CD conjugated on Self-peptide could significantly affect their secondary structure (Akiyoshi et al., 2000). Therefore, the interaction between $^{β-CD}$Self-peptide and YIGSR was confirmed, which for mixed $^{β-CD}$Self-peptide and YIGSR showed a significant decrease in helical content (Table S1), compared with the mixed Self-peptide and YIGSR. The interaction

between $^{β-CD}$Self-peptide and YIGSR was then confirmed by the Ad competition test. The $^{β-CD}$Self-peptide release from NPs was via an Ad-concentration-dependent manner (Figure S3D). Combined with the Ad-relevant viability test using three kinds of cell lines (NIH 3T3 fibroblast cells, MAD-MB-231 breast cancer cells, and HOS-MNNG osteosarcoma cells; Figure S3E), the adopted Ad concentration for reversing the self-mimicking on ^{Rev}SeMicNPs in the follow-up test was 10 μg mL^{-1}.
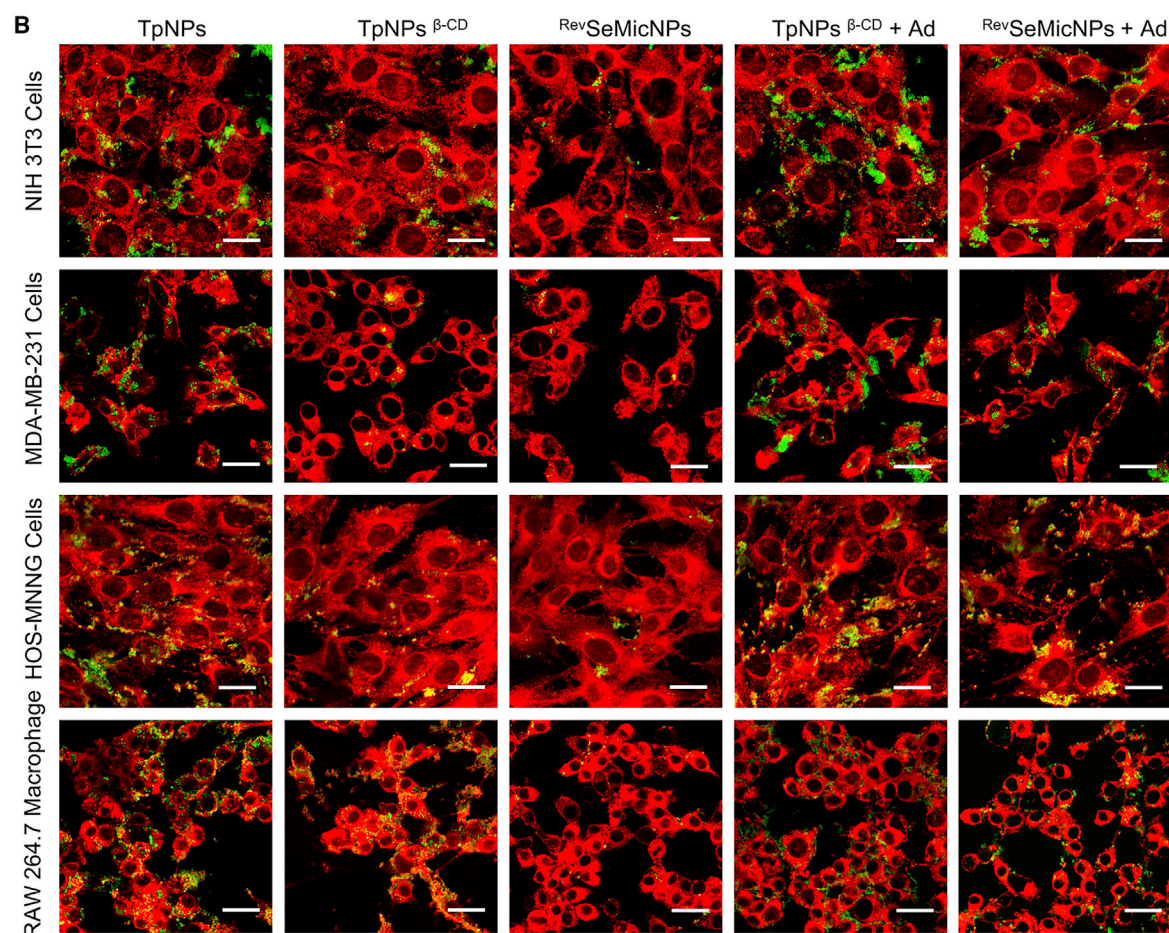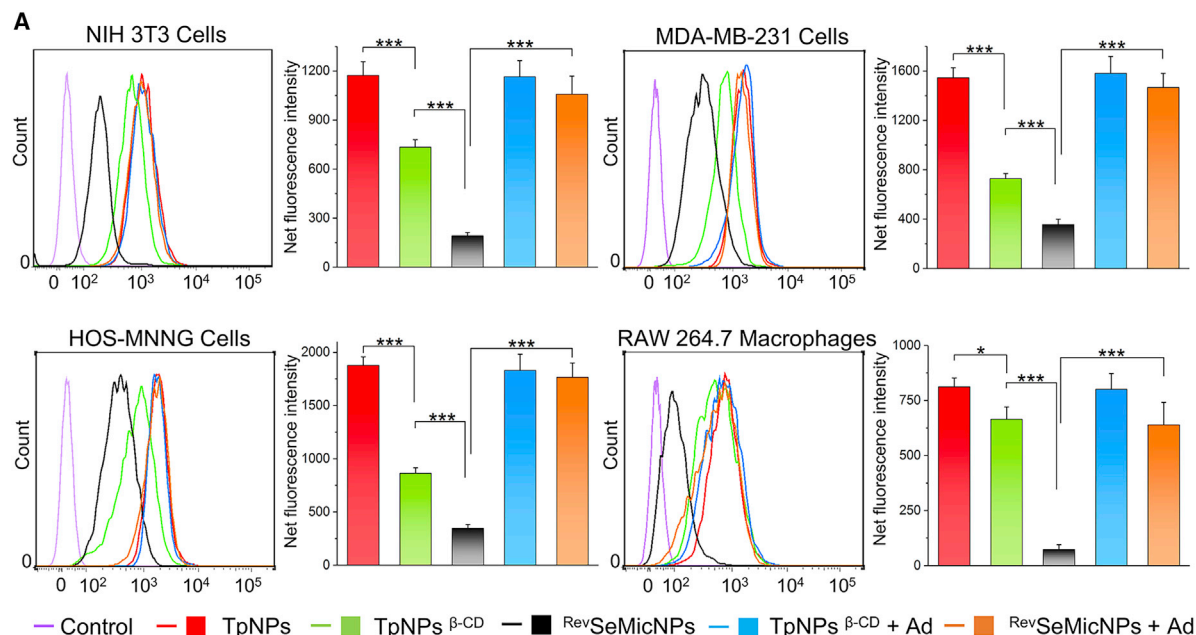
Because the surface charge and morphology can directly affect protein adsorption onto the surface of NPs, it was expected that the zwitterionic PEI-oligonucleotide-peptide surface can alleviate protein corona formation, which is favorable for reducing the immunogenicity and maintaining the autonomy of NPs (Ashraf et al., 2016; Almalik et al., 2017; Salvati et al., 2013). To verify this hypothesis, serum protein adsorption amount on the different kinds of prepared NPs was investigated with 10% human serum (Dai et al., 2014). In this comparison, the adsorbed protein amount of bare UnPSi was set as control (100%). As shown in Figure 1F, loading AS1411 and modifying Self-peptide can both significantly reduce the amount of protein adsorption. In addition, this pre-coated peptide corona may also have similar effect as pre-coated protein corona, which can shield from subsequent protein adsorption (Oh et al., 2018).

Next, the release profiles of 17-AAG were followed in human serum (Figure 1G). As a result of insufficient steric hindrance and electrostatic shielding effect from the serum proteins, drug loaded in TpNPs suffered from burst release, with ∼40% released in the first 15 min and nearly 80% released in 120 min. After modification with Self-peptide, the burst release effect was attenuated. However, more than 50% of the drug was still released in 4 h, after which the ^{Rev}SeMicNPs showed continuous release for the next 8 h. After loading AS1411, the drug release amount was restrained within 20% during the release period, suggesting that the dense, zwitterionic PEI-oligonucleotide-peptide surface of the NPs can efficiently avoid the interaction between the PSi pores and serum proteins. After adding Ad, the protective surface layer was disintegrated and the drug release showed a modest Ad-triggered burst release behavior, which lasted for 1 h, after which the drug showed slow and continuous release similar to ^{Rev}SeMicNPs.

Next, the biocompatibility of the different NPs was investigated using 3T3, MDA-MB-231, and HOS-MNNG cells (Figure S3F). Overall, the UnPSi-PEI NPs showed cytotoxicity due to the positive surface charge, but after PEG-YIGSR

Figure 1. Characterizations of the prepared NPs

(A) The starting and ending frame of molecular dynamic simulation trajectory.

(B) The detailed interaction between experimental Self-peptide and SIRPα interface by computational mimicking. Self-peptide (in cyan) and SIRPα (in green), with the key interface residues shown in stick mode.

(C) The predicted binding posed by computational docking of experimental Self-peptide to SIRPα: (a) the most likely binding pose in red; (b) and (c) other possible experimental peptide-binding poses in green and in blue individually.

(D) Hydrodynamic size, polydispersity index (PdI), and ζ-potential of the prepared NPs (data represent mean ± SD, n = 10).

(E) Transmission electron microscopy (TEM) images of the obtained NPs.

(F) Circular dichroism spectroscopic data of YIGSR peptide, Self-peptide, $^{β-CD}$Self peptide, an equimolar mixture of YIGSR peptide and Self peptide, and an equimolar mixture of YIGSR peptide and $^{β-CD}$Self-peptide.

(G) Human serum proteins adsorption onto the NPs after 1 h incubation at 37°C (data represent mean ± SD, n = 3; the significance level was set at probabilities of *p < 0.05, **p < 0.01, and ***p < 0.001).

(H) The cumulative release profile of 17-AAG from different types of NPs in 10% human serum (data represent mean ± SD, n = 3). Asterisk (*) means the initial point of amantadine-triggered release in the group of AS1411@^{Rev}SeMicNPs + Ad.

A

NIH 3T3 Cells · MDA-MB-231 Cells · HOS-MNNG Cells · RAW 264.7 Macrophages

Control · TpNPs · TpNPs $^{\beta\text{-CD}}$ · ^{Rev}SeMicNPs · TpNPs $^{\beta\text{-CD}}$ + Ad · ^{Rev}SeMicNPs + Ad

B

TpNPs · TpNPs $^{\beta\text{-CD}}$ · ^{Rev}SeMicNPs · TpNPs $^{\beta\text{-CD}}$ + Ad · ^{Rev}SeMicNPs + Ad

NIH 3T3 Cells · MDA-MB-231 Cells · HOS-MNNG Cells · RAW 264.7 Macrophage

(legend on next page)

modification, the PEI cytotoxicity was reduced. However, time- and concentration-dependent toxicity of TpNPs was still observed. By contrast, [Rev]SeMicNPs showed long-term biocompatibility even at high concentrations.

Before further investigating the mechanism, western blot was performed to determine the expression of SIRPα on the aforementioned cell lines, as well as the phagocyte of RAW 264.7 macrophages (Figure S4). It was observed that all the tested cells expressed SIRPα protein; however, the amounts in 3T3 cells and RAW 264.7 macrophages were higher than in the other cancer cells.

Multistage signal-interactive effect modulated NP-cell interactions *in vitro*

Next, as one of the key indices for evaluating the efficiency of NP-cell communication, targeting specificity of NPs with different signal interfaces and the off-target effect caused by grafting with targeting molecules was investigated (Dahlman et al., 2017; Yu et al., 2018). In this study, four types of cell lines (3T3, MDA-MB-231, and HOS-MNNG cells and RAW 264.7 macrophages) were used to evaluate the uptake amount by flow cytometry quantification. Five groups of different NPs—TpNPs (positive control), TpNPs capped by β-CD (for blocking the function of Tyr, termed as TpNPs[β-CD]), [Rev]SeMicNPs, TpNPs[β-CD] + Ad, and [Rev]SeMicNPs + Ad—were compared. For 3T3, MDA-MB-231, and HOS-MNNG cells, after blocking Tyr by β-CD, the fluorescence intensity showed a notable decrease, with an uptake inhibition ratio of 37.4, 52.8, and 54.0% for the three cell types, respectively. The uptake inhibition ratio of NPs that underwent [β-CD]Self-peptide blocking to the cells further increased to 83.6, 76.9, and 81.6%, respectively. By contrast, we found that β-CD blocking had limited effect to inhibit RAW 264.7 macrophage uptake compared with the other groups, whereas the inhibition ratio was only 18.3%, indicating that the β1-integrine-mediated endocytosis was not the major driving force for the uptake of NPs by macrophages (Kuhn et al., 2014; Behzadi et al., 2017). However, the inhibition effect of [Rev]SeMicNPs was more significant, which reached 91.2% for RAW 264.7 macrophages, suggesting that reducing the immunogenicity of NPs is more efficient than depriving the targeting capacity to shield from macrophage clearance. For both TpNPs[β-CD] and [Rev]SeMicNPs, inclusion of Ad can substantially recover the level of cell uptake efficiency to that of TpNPs, further suggesting the effectiveness of the multistage communication process for cell targeting modulation. The outcome of the flow cytometry experiments was further confirmed by confocal fluorescence imaging, and similar trends were found (Figure 2B).

Multistage signal-interactive NPs improved tumor targeting *in vivo*

As a result of the signal-interactive induced targeting selectivity data, an evaluation of the systematic time-dependent NPs'

biodistribution and accumulation was also performed *in vivo*, using the HOS-MNNG tumor-bearing nude mice model. Mice were subcutaneously injected with HOS-MNNG cells to form a xenograft tumor. To test the tumor-targeting capacity of the designed NPs, TpNPs and [Rev]SeMicNPs loaded with AS1411 to form a zwitterionic surface to avoid the interference of protein corona were conjugated with Cy 7.5 for near-IR fluorescence tracing. After injection by tail vein, 6 time points (3, 6, 12, 24, 48, and 72 h) were used to investigate the real-time biodistribution of the NPs (Figures 3A and 3B). Overall, the TpNPs-treated mice showed clear fluorescence signal all over the body, with the highest fluorescence intensity in liver. The fluorescence intensity did not display reduction over the duration of the experiment, indicating the non-interactive NPs had limited specificity and long-term accumulation behavior. In addition, the tumor accumulation of the NPs did not show an increase even after 72 h. By contrast, the [Rev]SeMicNPs showed significant difference of distribution behavior in the mice. During the first 3 h, specific accumulation in the tumor was observed, and the relevant fluorescence intensity was already higher than in the liver. Furthermore, the tumor-site-related fluorescence intensity enhanced over time, suggesting the continuous accumulation behavior of the NPs. Moreover, the fluorescence intensity in liver presented a reducing tendency, indicating that unlike the TpNPs, which are rapidly sequestered by the liver, [Rev]SeMicNPs with self-mimicking mechanism have efficient liver-escaping capacity. Taking advantage of the limited liver sequestration and enhanced tumor accumulation over time, [Rev]SeMicNPs demonstrated significant tumor specificity after 72 h.

The investigation of organ accumulation of NPs was then used to quantify the amount of NPs for statistical comparison (Figures 3C and 3D, the sequence of the organs' placement is heart, liver, spleen, lung, kidney, and tumor). The related average radiant efficiency (avgRE) of the test organs is shown in Figure 3E. For three time points (6, 48, and 72 h), the ratio of tumor-to-liver (ratio[tumor/liver]) accumulation was used to determine tumor-specific targeting of the NPs. Inconsistent with the real-time biodistribution, the accumulation of NPs for the TpNPs group did not show notable time-dependent changes as a result of fast liver sequestration. The ratio[tumor/liver] at 6, 48, and 72 h was 0.45, 0.40, and 0.37, respectively, whereas for the [Rev]SeMicNPs groups, the corresponding ratio was 0.92, 1.45, and 2.06, respectively. Compared with the groups in same time point, the fluorescence intensity of tumor accumulation in [Rev]SeMicNPs groups was 1.3, 2.3, and 2.8 times of that in TpNPs groups, whereas the relevant amount of liver accumulation in [Rev]SeMicNPs groups was 65, 62, and 51% of that in TpNPs groups. These comparisons demonstrated that not only at an early time but also after long-term accumulation, the NPs with communication mechanism showed reduced liver retention and enhanced tumor accumulation unlike the non-interactive NPs. It is worth noting that for [Rev]SeMicNPs groups, although

---

Figure 2. Investigation of the NP-cell interactions *in vitro*

(A) Flow cytometry quantitative analysis of cell uptake efficiency to NPs in Hank's balanced salt solution (HBSS) buffer (1×, pH 7.4) (data represent mean ± SD, n = 3; the significance level was set at probabilities of *p < 0.05, **p < 0.01, and ***p < 0.001).

(B) Confocal fluorescence microscopy images of cells (red: cell membranes stained with CellMask Deep Red; green: fluorescein isothiocyanate (FITC)-labeled NPs; yellow: co-localization of the NPs and the cell membrane; scale bar, 20 μm).
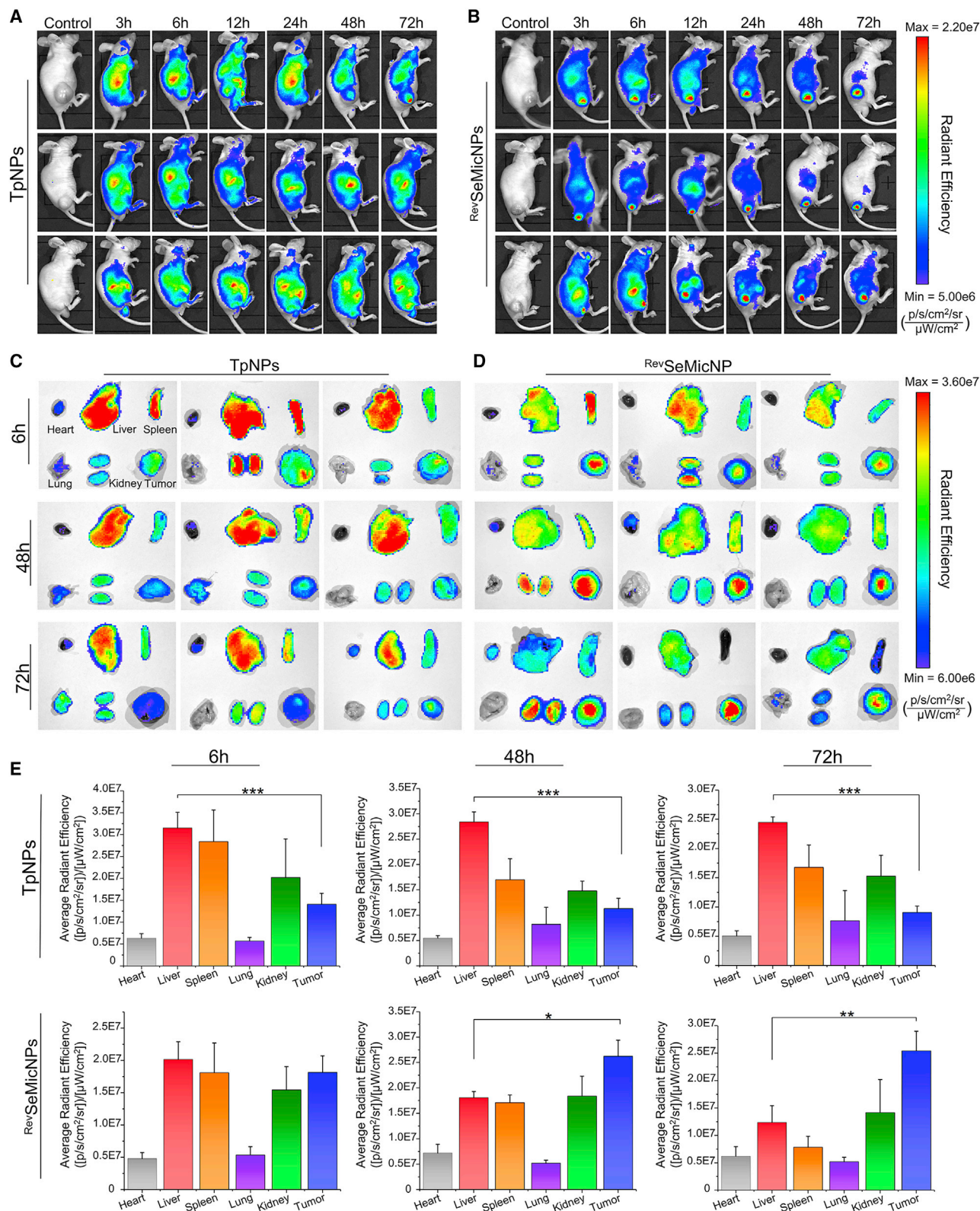
the ratio$_{tumor/liver}$ was continuously increasing within 72 h, the reduced avgRE of tumor at 72 h indicated that the amount of accumulated NPs was less than that at 48 h. Thus, we chose 72 h as the time point for Ad injection, which will subsequently induce the particle transformation into the active form for tumor therapy. Furthermore, in view of the limited differences in size and surface charge between the two types of NPs, it is reasonable to attribute this change in the behaviors of biodistribution and hepatic clearance to the different surface properties.

Antitumor efficacy and safety evaluation

For *in vivo* safety evaluation, blood tests of white blood cells (WBCs), red blood cells (RBCs), hemoglobin (HGB), and platelets (PLTs); liver function tests of alanine aminotransferase (ALT), aspartate aminotransferase (AST), alkaline phosphatase (ALP), and gamma-glutamyl transpeptidase (GGT); and kidney function tests of creatinine (CRE) and blood urea nitrogen (BUN) were performed to evaluate the acute toxicity at 24 h post-injection (Figures 4A and 4B). As a result of the good biocompatibility of the ^{Rev}SeMicNPs, we chose 100 μg mL^{-1} as the test concentration. Overall, the ^{Rev}SeMicNPs-treated mice showed no obvious difference in all tested indices compared with control group, expect GGT. The group treated with TpNPs showed abnormal indicator in several indices, however, not as significant as that in the cell viability test. Especially, the decrease of RBCs and PLTs indicated hemolytic toxicity. In addition, TpNPs induced higher liver function index of ALT and AST, which indicates liver damage or inflammation. Especially, the increase of ALT implies mitochondrial damage of liver cells. By contrast, these abnormal indicators were not observed in the ^{Rev}SeMicNPs group, suggesting that self-mimicking can improve the safety of the NPs for *in vivo* applications.

In the antiproliferation test (Figure 4C), all the agents followed dosage- and time-dependent therapeutic performance. Overall, the performance of drug-loaded TpNPs (drug@TpNPs) was better than that of other groups of free drugs, especially after long-time incubation (48 h). The drug-loaded ^{Rev}SeMicNPs (drug@^{Rev}SeMicNPs) showed differentiable "on" and "off" cytotoxic behavior with/without the Ad signal. As a result of the synergetic effect of targeting depriving and self-mimicking endowed by chimeric peptide interface, ^{Rev}SeMicNPs were difficult to uptake by cells compared with TpNPs. Thus, the cytotoxicity of ^{Rev}SeMicNPs was in the "off" state. After Ad triggering, NPs converted into the targeting-active form for efficient cell uptake and then the cytotoxicity came into "on" state. This is another proof that the introduction of multistage signal-interactive mechanism on NPs is very promising for targeted cancer treatment with low risks of systemic toxicity.

Next, the antitumor investigation of the NPs was performed. Based on previous study on *in vivo* toxicity of the NPs and the antiproliferation test, a nanosystem at 100 μg mL^{-1} was used as the test concentration. When the volume of the solid tumor reached approximately 100 mm^3, the mice received

different treatments: saline; 17-AAG only; AS1411 only; 17-AAG + AS1411; and drug@TpNPs, drug@^{Rev}SeMicNPs, and drug@^{Rev}SeMicNPs with Ad intravenous injection after 72 h. The tumors were extracted from the mice after a 35-day treatment (Figure 4D), and the tumor volume was monitored during this period. As shown in Figure 4E, the volume of tumors treated with saline increased greatly and was approximately 46-fold larger than its initial volume. The 17-AAG and AS1411 combination showed a synergistic effect, and the tumor volume was found to increase only 8.3-fold over this period compared with 15.8-fold when treated only with 17-AAG, although the synergistic effect was not obvious in cell study. While the drug-loaded TpNPs had better antitumor activity at an early stage than 17-AAG + AS1411, no statistical difference was observed at the end of the test. It is worth mentioning that the tumors treated by TpNPs had an accelerating growth speed (Figure S5A). This may be attributed to the accelerated blood clearance effect to the NPs (Ishihara et al., 2009; Ishida et al., 2005). Without triggering the active targeting, drug-loaded ^{Rev}SeMicNPs showed a similar therapeutic effect as drug-loaded TpNPs. After combining with Ad, the tumors treated with drug-loaded ^{Rev}SeMicNPs + Ad showed significant tumor growth inhibition, of which tumors in two mice were even fully eliminated, suggesting maximized therapeutic efficacy by the enhanced tumor accumulation and the subsequent targeting activation. The statistical analysis of final tumor weight is shown in Figure S5B. The antitumor effect of the NPs without drug loading was then investigated (Figures S5C and S5D). Generally, both TpNPs and ^{Rev}SeMicNPs showed minor therapeutical effect. For ^{Rev}SeMicNPs, this is attributed to the good biocompatibility and homeostasis, reducing cell uptake; for TpNPs, it is attributed to the limited tumor accumulation. Moreover, the ^{Rev}SeMicNPs + Ad group showed better antitumor efficacy, indicating that efficient tumor accumulation by reversible self-mimicking and *in situ* particle transformation can amplify the cytotoxicity of TpNPs. However, the therapeutic efficacy was limited compared with the drug-loaded NPs.

Hematoxylin and eosin (H&E) staining with the five major organs (heart, liver, spleen, lung, and kidney) and the tumor was also conducted to further evaluate the safety and therapeutic efficacy of the NPs (Figure S5E). First, as a major organ of mononuclear phagocyte system, liver sections were used to investigate the toxicity caused by accumulation of different therapeutics (Figure 4F). Significant hepatic injury was observed in the drug@TpNPs-treated groups, and the injury degree was higher than that of the combined drug group, indicating the significant liver accumulation of NPs. By contrast, the self-mimicking NPs showed distinguishable safety as no obvious nuclear shrinkage or fragmentation was presented. On the other hand, the ^{Rev}MicNPs + Ad group showed increased safety risk, however, better than that of the combined drug group. This can be attributed to the NPs remaining in the liver that converted into the form of TpNPs after Ad triggering, which still have cumulative

---

Figure 3. Investigation of the tumor targeting efficiency *in vivo*
Systemic time-dependent biodistribution of TpNPs (A) and ^{Rev}SeMicNPs (B). *In vivo* imaging of five major organs and tumors harvested from mice at 6, 48, and 72 h post-injection with TpNPs (C) or ^{Rev}SeMicNPs (D). The average fluorescence intensity of the five major organs and tumor (E) (data represent mean ± SD, n = 3; the significance level was set at probabilities of *p < 0.05, **p < 0.01, and ***p < 0.001).
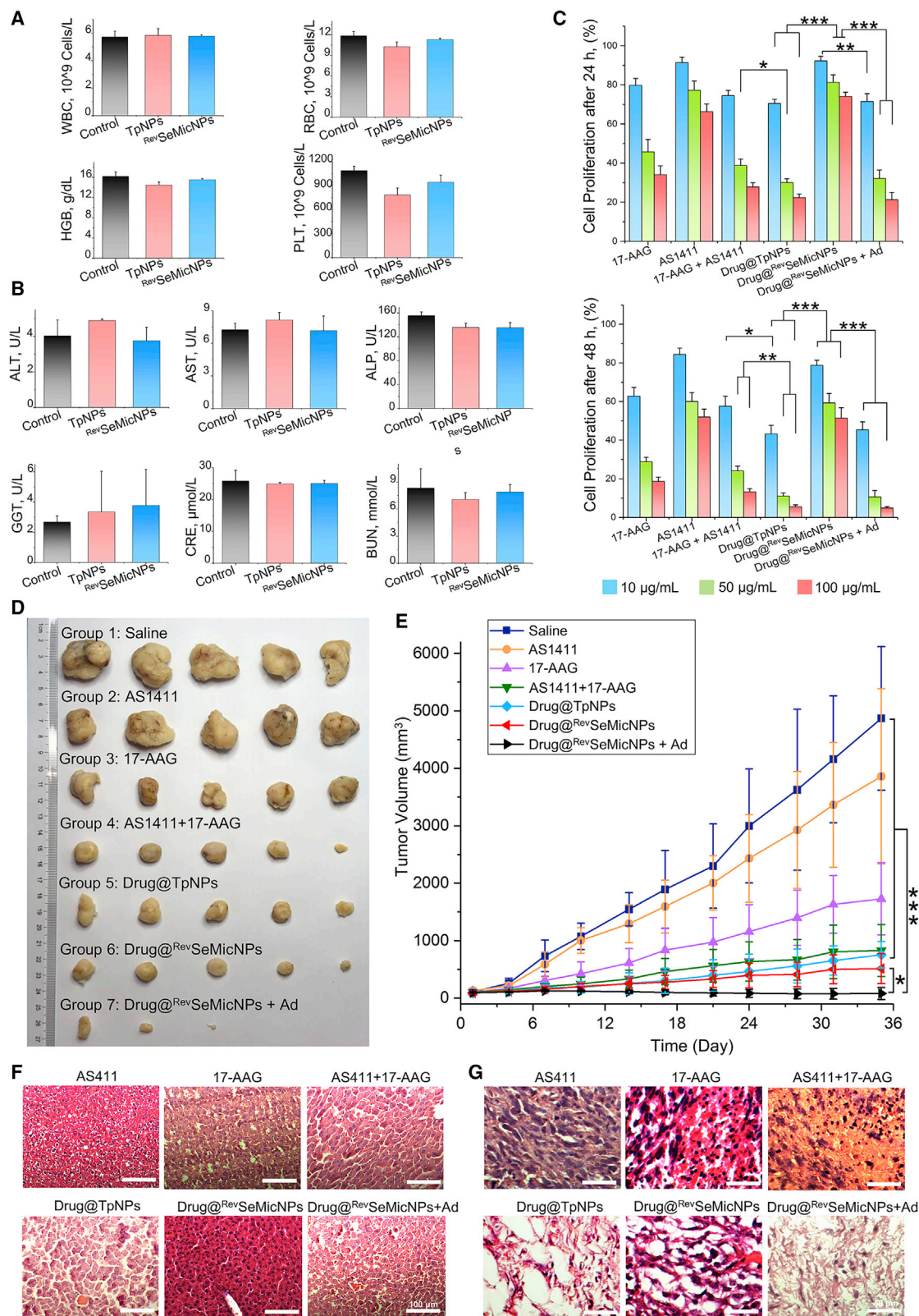
(legend on next page)

toxicity in the liver. This follow-up cytotoxicity increase can be circumvented by optimizing the time of Ad triggering after a better understanding of the biodistribution of NPs. Finally, the H&E staining on tumor sections demonstrated that all types of the NP-based therapeutics can cause extensive apoptosis in tumor cells (Figure 4G).

DISCUSSION

In conclusion, we evaluated the targeting problem of NPs from the perspective of communication-determined homeostasis and developed a multistage signal-interactive system to promote the efficiency of the NP-cell communications. By introducing an interactive mechanism, the tumor-targeting capacity of NPs can be improved by almost 3-fold, while the liver accumulation can be reduced by nearly 50%. Accordingly, the tumor weight after treatment by signal-interactive NPs is only 15.4% of the control with obviously restricted hepatic damage. We proved this pattern of multistage signal-interactive system can efficiently integrate various types of signal modules and improve the autonomy-determined homeostasis of NPs. It can be expected that the concept of "communication system" will emerge as a promising platform for multivariate integration and regulation of bio-signals, which means the treatment patterns can be determined by the type of NP-cell communication, and NPs can deeply participate in cell communications and their biological behavior. We anticipate this strategy can inspire construction of more powerful therapeutic systems to promote the clinical transition of nanomedicines.

STAR★METHODS

Detailed methods are provided in the online version of this paper and include the following:

- KEY RESOURCES TABLE
- RESOURCE AVAILABILITY
  - Lead contact
  - Materials availability
  - Data and code availability
- EXPERIMENTAL MODEL AND SUBJECT DETAILS
- METHOD DETAILS
  - Synthesize of β-CD-BCN
  - Synthesize of peptides
  - Synthesize of β-CD-Self-peptides
  - ^{1}H NMR spectra
  - MALDI-TOF mass spectra
  - LCMS analysis
  - CD spectra
  - HPLC purifications of peptides
  - Peptide docking
  - Preparation of UnTHCPSi NPs
  - Fabrication of the multistage signal interactive system
  - Characterization of the NPs
  - Protein adsorption of the NPs
  - Drug loading degree
  - Helical content detecting
  - Cell culturing
  - Western-blotting
  - *In vitro* cytotoxicity
  - Confocal fluorescence microscopy imaging
  - Cell uptake flow cytometry analysis
  - Cell growth inhibition
  - Biodistribution investigation
  - *In vivo* NIRF imaging
  - *Ex vivo* histological staining
- QUANTIFICATION AND STATISTICAL ANALYSIS

SUPPLEMENTAL INFORMATION

Supplemental information can be found online at https://doi.org/10.1016/j.celrep.2021.109131.

AUTHOR CONTRIBUTIONS

H.A.S., W.C., and H.Z. conceived the project and guided the experiments. F.Z. designed the experiments, performed most of the synthesis experiments and *in vitro* cell experiments, participated in all *in vivo* experiments, and wrote the manuscript. Yiran Zhang and H.L. performed most of the animal experiment. L.K. prepared and characterized the functional peptide. Yuezhou Zhang performed the computer modeling and docking. E.M. prepared the UnPSi NPs. J.S., J.T.H, Yueqi Zhu, Y.C., L.D., and A.K. guided the experiments.

DECLARATION OF INTERESTS

The authors declare no competing interests.

Figure 4. Antitumor efficacy and safety evaluation
(A and B) Safety evaluation through blood routine test of WBCs, RBCs, HGB, and TLP (A); liver function test of ALT, AST, ALP, and GGT; and kidney function test of CRE and urea (B) (data represent mean ± SD, n = 3).
(C) Cancer cell growth inhibition by treatment of HOS-MNNG cells (data represent mean ± SD, n = 3; the significance level was set at probabilities of *p < 0.05, **p < 0.01, and ***p < 0.001).
(D) The image of HOS-MNNG tumors resected after the last treatment.
(E) Tumor volume curves of mice treated with different formulations (data represent mean ± SD, n = 5; the significance level was set at probabilities of *p < 0.05, **p < 0.01, and ***p < 0.001).
(F) H&E staining of livers in mice that received different treatments.
(G) H&E staining of tumors in mice that received different treatments.

Cell Reports
Report

CellPress
OPEN ACCESS

REFERENCES

Akiyoshi, K., Ueminami, A., Kurumada, S., and Nomura, Y. (2000). Self-Association of Cholesteryl-Bearing Poly(l-lysine) in Water and Control of Its Secondary Structure by Host−Guest Interaction with Cyclodextrin. Macromolecules 33, 6752–6756.

Almalik, A., Benabdelkamel, H., Masood, A., Alanazi, I.O., Alradwan, I., Majrashi, M.A., Alfadda, A.A., Alghamdi, W.M., Alrabiah, H., Tirelli, N., and Alhasan, A.H. (2017). Hyaluronic Acid Coated Chitosan Nanoparticles Reduced the Immunogenicity of the Formed Protein Corona. Sci. Rep. 7, 10542.

Ashraf, S., Park, J., Bichelberger, M.A., Kantner, K., Hartmann, R., Maffre, P., Said, A.H., Feliu, N., Lee, J., Lee, D., et al. (2016). Zwitterionic surface coating of quantum dots reduces protein adsorption and cellular uptake. Nanoscale 8, 17794–17800.

Behzadi, S., Serpooshan, V., Tao, W., Hamaly, M.A., Alkawareek, M.Y., Dreaden, E.C., Brown, D., Alkilany, A.M., Farokhzad, O.C., and Mahmoudi, M. (2017). Cellular uptake of nanoparticles: journey inside the cell. Chem. Soc. Rev. 46, 4218–4244.

Bertrand, N., Grenier, P., Mahmoudi, M., Lima, E.M., Appel, E.A., Dormont, F., Lim, J.M., Karnik, R., Langer, R., and Farokhzad, O.C. (2017). Mechanistic understanding of in vivo protein corona formation on polymeric nanoparticles and impact on pharmacokinetics. Nat. Commun. 8, 777.

Bimbo, L.M., Sarparanta, M., Santos, H.A., Airaksinen, A.J., Mäkilä, E., Laaksonen, T., Peltonen, L., Lehto, V.P., Hirvonen, J., and Salonen, J. (2010). Biocompatibility of thermally hydrocarbonized porous silicon nanoparticles and their biodistribution in rats. ACS Nano 4, 3023–3032.

Blanco, E., Shen, H., and Ferrari, M. (2015). Principles of nanoparticle design for overcoming biological barriers to drug delivery. Nat. Biotechnol. 33, 941–951.

Bloemendal, S., and Kück, U. (2013). Cell-to-cell communication in plants, animals, and fungi: a comparative review. Naturwissenschaften 100, 3–19.

Bodelón, G., Costas, C., Pérez-Juste, J., Pastoriza-Santos, I., and Liz-Marzán, L.M. (2017). Gold nanoparticles for regulation of cell function and behavior. Nano Today 13, 40–60.

Bouhadiba, A., Belhocine, Y., Rahim, M., Djilani, I., Nouar, L., and Khatmi, D.E. (2017). Host-guest interaction between tyrosine and β-cyclodextrin: Molecular modeling and nuclear studies. J. Mol. Liq. 233, 358–363.

Bray, D. (1998). Signaling complexes: biophysical constraints on intracellular communication. Annu. Rev. Biophys. Biomol. Struct. 27, 59–75.

Chen, G., and Jiang, M. (2011). Cyclodextrin-based inclusion complexation bridging supramolecular chemistry and macromolecular self-assembly. Chem. Soc. Rev. 40, 2254–2266.

Corbo, C., Molinaro, R., Parodi, A., Toledano Furman, N.E., Salvatore, F., and Tasciotti, E. (2016). The impact of nanoparticle protein corona on cytotoxicity, immunotoxicity and target drug delivery. Nanomedicine (Lond.) 11, 81–100.

Dahlman, J.E., Kauffman, K.J., Xing, Y., Shaw, T.E., Mir, F.F., Dlott, C.C., Langer, R., Anderson, D.G., and Wang, E.T. (2017). Barcoded nanoparticles for high throughput in vivo discovery of targeted therapeutics. Proc. Natl. Acad. Sci. USA 114, 2060–2065.

Dai, Q., Walkey, C., and Chan, W.C.W. (2014). Polyethylene glycol backfilling mitigates the negative impact of the protein corona on nanoparticle cell targeting. Angew. Chem. Int. Ed. Engl. 53, 5093–5096.

Devaraj, N.K. (2018). The Future of Bioorthogonal Chemistry. ACS Cent. Sci. 4, 952–959.

Dvir, T., Banghart, M.R., Timko, B.P., Langer, R., and Kohane, D.S. (2010). Photo-targeted nanoparticles. Nano Lett. 10, 250–254.

Feliu, N., Docter, D., Heine, M., Del Pino, P., Ashraf, S., Kolosnjaj-Tabi, J., Macchiarini, P., Nielsen, P., Alloyeau, D., Gazeau, F., et al. (2016). In vivo degeneration and the fate of inorganic nanoparticles. Chem. Soc. Rev. 45, 2440–2457.

Friesner, R.A., Banks, J.L., Murphy, R.B., Halgren, T.A., Klicic, J.J., Mainz, D.T., Repasky, M.P., Knoll, E.H., Shelley, M., Perry, J.K., et al. (2004). Glide: a new approach for rapid, accurate docking and scoring. 1. Method and assessment of docking accuracy. J. Med. Chem. 47, 1739–1749.

Gianti, E., and Zauhar, R.J. (2015). An SH2 domain model of STAT5 in complex with phospho-peptides define "STAT5 Binding Signatures". J. Comput. Aided Mol. Des. 29, 451–470.

Graf, J., Ogle, R.C., Robey, F.A., Sasaki, M., Martin, G.R., Yamada, Y., and Kleinman, H.K. (1987). A pentapeptide from the laminin B1 chain mediates cell adhesion and binds the 67,000 laminin receptor. Biochemistry 26, 6896–6900.

Gustafson, H.H., Holt-Casper, D., Grainger, D.W., and Ghandehari, H. (2015). Nanoparticle uptake: The phagocyte problem. Nano Today 10, 487–510.

Hu, Q.D., Tang, G.P., and Chu, P.K. (2014). Cyclodextrin-based host-guest supramolecular nanoparticles for delivery: from design to applications. Acc. Chem. Res. 47, 2017–2025.

Ishida, T., Harada, M., Wang, X.Y., Ichihara, M., Irimura, K., and Kiwada, H. (2005). Accelerated blood clearance of PEGylated liposomes following preceding liposome injection: effects of lipid dose and PEG surface-density and chain length of the first-dose liposomes. J. Control. Release 105, 305–317.

Ishihara, T., Takeda, M., Sakamoto, H., Kimoto, A., Kobayashi, C., Takasaki, N., Yuki, K., Tanaka, K., Takenaga, M., Igarashi, R., et al. (2009). Accelerated blood clearance phenomenon upon repeated injection of PEG-modified PLA-nanoparticles. Pharm. Res. 26, 2270–2279.

Jiang, R.J., Zhao, Y.L., Chen, Y.J., Xiao, D., Wang, F., Han, B., Yang, J., Liao, X.L., Yang, L.J., Gao, C.Z., and Yang, B. (2014). Synthesis, characterization, and in vitro evaluation of artesunate-β-cyclodextrin conjugates as novel anticancer prodrugs. Carbohydr. Res. 400, 19–25.

Kuhn, D.A., Vanhecke, D., Michen, B., Blank, F., Gehr, P., Petri-Fink, A., and Rothen-Rutishauser, B. (2014). Different endocytotic uptake mechanisms for nanoparticles in epithelial cells and macrophages. Beilstein J. Nanotechnol. 5, 1625–1636.

Lai, W.F., Rogach, A.L., and Wong, W.T. (2017). Chemistry and engineering of cyclodextrins for molecular imaging. Chem. Soc. Rev. 46, 6379–6419.

Li, W., Liu, Z., Fontana, F., Ding, Y., Liu, D., Hirvonen, J.T., and Santos, H.A. (2018). Tailoring Porous Silicon for Biomedical Applications: From Drug Delivery to Cancer Immunotherapy. Adv. Mater. 30, e1703740.

Li, Z., Xiao, C., Yong, T., Li, Z., Gan, L., and Yang, X. (2020). Influence of nanomedicine mechanical properties on tumor targeting delivery. Chem. Soc. Rev. 49, 2273–2290.

Lundqvist, M., Stigler, J., Elia, G., Lynch, I., Cedervall, T., and Dawson, K.A. (2008). Nanoparticle size and surface properties determine the protein corona with possible implications for biological impacts. Proc. Natl. Acad. Sci. USA 105, 14265–14270.

Moghimi, S.M., and Simberg, D. (2017). Complement activation turnover on surfaces of nanoparticles. Nano Today 15, 8–10.

Mohammadinejad, R., Moosavi, M.A., Tavakol, S., Vardar, D.Ö., Hosseini, A., Rahmati, M., Dini, L., Hussain, S., Mandegary, A., and Klionsky, D.J. (2019). Necrotic, apoptotic and autophagic cell fates triggered by nanoparticles. Autophagy 15, 4–33.

Mondal, B.C., Mukherjee, T., Mandal, L., Evans, C.J., Sinenko, S.A., Martinez-Agosto, J.A., and Banerjee, U. (2011). Interaction between differentiating cell- and niche-derived signals in hematopoietic progenitor maintenance. Cell 147, 1589–1600.

Noireaux, V., Maeda, Y.T., and Libchaber, A. (2011). Development of an artificial cell, from self-organization to computation and self-reproduction. Proc. Natl. Acad. Sci. USA 108, 3473–3480.

Oh, J.Y., Kim, H.S., Palanikumar, L., Go, E.M., Jana, B., Park, S.A., Kim, H.Y., Kim, K., Seo, J.K., Kwak, S.K., et al. (2018). Cloaking nanoparticles with protein corona shield for targeted drug delivery. Nat. Commun. 9, 4548.

Peer, D., Karp, J.M., Hong, S., Farokhzad, O.C., Margalit, R., and Langer, R. (2007). Nanocarriers as an emerging platform for cancer therapy. Nat. Nanotechnol. 2, 751–760.

Perbal, B. (2003). Communication is the key. Cell Commun. Signal. 1, 3.

Rabe, M., Boyle, A., Zope, H.R., Versluis, F., and Kros, A. (2015). Determination of oligomeric states of peptide complexes using thermal unfolding curves. Biopolymers 104, 65–72.

Rodriguez, P.L., Harada, T., Christian, D.A., Pantano, D.A., Tsai, R.K., and Discher, D.E. (2013). Minimal "Self" peptides that inhibit phagocytic clearance and enhance delivery of nanoparticles. Science 339, 971–975.

Rosenblum, D., Joshi, N., Tao, W., Karp, J.M., and Peer, D. (2018). Progress and challenges towards targeted delivery of cancer therapeutics. Nat. Commun. 9, 1410.

Sadelain, M., Brentjens, R., and Rivière, I. (2013). The basic principles of chimeric antigen receptor design. Cancer Discov. 3, 388–398.

Salehi-Reyhani, A., Ces, O., and Elani, Y. (2017). Artificial cell mimics as simplified models for the study of cell biology. Exp. Biol. Med. (Maywood) 242, 1309–1317.

Salvati, A., Pitek, A.S., Monopoli, M.P., Prapainop, K., Bombelli, F.B., Hristov, D.R., Kelly, P.M., Åberg, C., Mahon, E., and Dawson, K.A. (2013). Transferrin-functionalized nanoparticles lose their targeting capabilities when a biomolecule corona adsorbs on the surface. Nat. Nanotechnol. 8, 137–143.

Sarfati, G., Dvir, T., Elkabets, M., Apte, R.N., and Cohen, S. (2011). Targeting of polymeric nanoparticles to lung metastases by surface-attachment of YIGSR peptide from laminin. Biomaterials 32, 152–161.

Scott, D.E., Bayly, A.R., Abell, C., and Skidmore, J. (2016). Small molecules, big targets: drug discovery faces the protein-protein interaction challenge. Nat. Rev. Drug Discov. 15, 533–550.

Shanmugam, M., Ramesh, D., Nagalakshmi, V., Kavitha, R., Rajamohan, R., and Stalin, T. (2008). Host-guest interaction of L-tyrosine with β-cyclodextrin. Spectrochim. Acta A Mol. Biomol. Spectrosc. 71, 125–132.

Shi, J., Kantoff, P.W., Wooster, R., and Farokhzad, O.C. (2017). Cancer nanomedicine: progress, challenges and opportunities. Nat. Rev. Cancer 17, 20–37.

Smiljanic, N., Moreau, V., Yockot, D., Benito, J.M., García Fernández, J.M., and Djedaïni-Pilard, F. (2006). Supramolecular control of oligosaccharide-protein interactions: switchable and tunable ligands for concanavalin A based on β-cyclodextrin. Angew. Chem. Int. Ed. Engl. 45, 5465–5468.

Tang, R., Moyano, D.F., Subramani, C., Yan, B., Jeoung, E., Tonga, G.Y., Duncan, B., Yeh, Y.-C., Jiang, Z., Kim, C., and Rotello, V.M. (2014). Rapid coating of surfaces with functionalized nanoparticles for regulation of cell behavior. Adv. Mater. 26, 3310–3314.

Toomari, Y., Namazi, H., and Akbar, E.A. (2015). Synthesis of the dendritic type β-cyclodextrin on primary face via click reaction applicable as drug nanocarrier. Carbohydr. Polym. 132, 205–213.

Trappmann, B., Gautrot, J.E., Connelly, J.T., Strange, D.G.T., Li, Y., Oyen, M.L., Cohen Stuart, M.A., Boehm, H., Li, B., Vogel, V., et al. (2012). Extracellular-matrix tethering regulates stem-cell fate. Nat. Mater. 11, 642–649.

Tsoi, K.M., MacParland, S.A., Ma, X.Z., Spetzler, V.N., Echeverri, J., Ouyang, B., Fadel, S.M., Sykes, E.A., Goldaracena, N., Kaths, J.M., et al. (2016). Mechanism of hard-nanomaterial clearance by the liver. Nat. Mater. 15, 1212–1221.

Tubert-Brohman, I., Sherman, W., Repasky, M., and Beuming, T. (2013). Improved docking of polypeptides with Glide. J. Chem. Inf. Model. 53, 1689–1699.

Wilhelm, S., Tavares, A.J., Dai, Q., Ohta, S., Audet, J., Dvorak, H.F., and Chan, W.C.W. (2016). Analysis of nanoparticle delivery to tumours. Nat. Rev. Mater. 1, 16014.

Yang, B., Chen, Y., and Shi, J. (2019). Nanocatalytic Medicine. Adv. Mater. 31, e1901778.

Yu, Z., Ge, Y., Sun, Q., Pan, W., Wan, X., Li, N., and Tang, B. (2018). A pre-protective strategy for precise tumor targeting and efficient photodynamic therapy with a switchable DNA/upconversion nanocomposite. Chem. Sci. (Camb.) 9, 3563–3569.

Zhang, F., Correia, A., Mäkilä, E., Li, W., Salonen, J., Hirvonen, J.J., Zhang, H., and Santos, H.A. (2017). Receptor-Mediated Surface Charge Inversion Platform Based on Porous Silicon Nanoparticles for Efficient Cancer Cell Recognition and Combination Therapy. ACS Appl. Mater. Interfaces 9, 10034–10046.

Zheng, T., Voskuhl, J., Versluis, F., Zope, H.R., Tomatsu, I., Marsden, H.R., and Kros, A. (2013). Controlling the rate of coiled coil driven membrane fusion. Chem. Commun. (Camb.) 49, 3649–3651.

Zhu, M., Gao, L., Li, X., Liu, Z., Xu, C., Yan, Y., Walker, E., Jiang, W., Su, B., Chen, X., and Lin, H. (2009). The analysis of the drug-targets based on the topological properties in the human protein-protein interaction network. J. Drug Target. 17, 524–532.

STAR★METHODS

KEY RESOURCES TABLE

REAGENT or RESOURCE	SOURCE	IDENTIFIER
Antibodies		
SIRP alpha Rabbit Polyclonal Antibody	Thermofisher Scientific, China	AB_2547020
HRP Monoclonal Antibody	Invitrogen	Cat# MA5-15367; AB_10984341
Chemicals, peptides, and recombinant proteins		
Polyethylenimine, PEI	Sigma-Aldrich	Cat# 408727
N-Ethyl-N'-(3-dimethylaminopropyl) carbodiimide, EDC	Sigma-Aldrich	Cat# 39391
1-Hydroxy-2,5-pyrrolidinedione, NHS	Sigma-Aldrich	Cat# 130672
6-mono(p-toluenesulfonyl)-β-cyclodextrin, β-CD-OTs	Cyclodextrin-Shop	Cat# CDexB-050
N-[(1R,8S,9 s)-Bicyclo[6.1.0]non-4-yn-9-ylmethyloxycarbonyl]-1,8-diamino-3,6-dioxaoctane, BCN-amine	Sigma-Aldrich	Cat# 745073
N_3-PEG_4-COOH	Iris-biotech	N/A
N,N,N',N'-Tetramethyl-O-(6-chloro-1H-benzotriazol-1-yl)uronium hexafluorophosphate, HCTU	Sigma Aldrich	Cat# 04936
Fmoc-Gly-OH	Novabiochem	Cat# 852001
Fmoc-Tyr(tBu)-OH	Novabiochem	Cat# 852020
Fmoc-Ile-OH	Novabiochem	Cat# 852010
Fmoc-Ser(tBu)-OH	Novabiochem	Cat# 852019
Fmoc-Arg(Pbf)-OH	Novabiochem	Cat# 852067
Fmoc-Thr(tBu)-OH	Novabiochem	Cat# 852000
Fmoc-Cys(Trt)-OH	Novabiochem	Cat# 852008
Fmoc-Glu(OtBu)-OH	Novabiochem	Cat# 852009
Fmoc-Val-OH	Novabiochem	Cat# 852021
Fmoc-Leu-OH	Novabiochem	Cat# 852011
Fmoc-Lys(Boc)-OH	Novabiochem	Cat# 852012
Fmoc-Lys(Mtt)-OH	Novabiochem	Cat# 852065
BCN-PEG4-NHS (ENDO)	Conju-Probe	N/A
Tanespimycin (17-AAG)	ShangHai Haoran Biological Technology CO. (China)	N/A
Sieber Amide resin	Chem-Impex International	Cat# 03541
Experimental models: cell lines		
MDA-MB-231 breast carcinoma cells	ATCC	HTB-26
NIH 3T3 fibroblast cells	ATCC	CRL-1658
RAW 264.7 macrophages	ATCC	TIB-71
HOS-MNNG cells	ATCC	CRL-1547
Experimental models: organisms/strains		
BALB/c mice	Zhejiang Academy of Medical Sciences	Male mice (4-week-old, 20 ± 2g) under SPF condition. Approved by the Institutional Animal Care and Use Committee of Ruijin Hospital (SYXK2018-0027)

Continued

REAGENT or RESOURCE	SOURCE	IDENTIFIER
Oligonucleotides		
AS1411, 5′-GGTGGTGGTGGTTGTGGTGGTGGTGG-3′	Sangon Biotech (Shanghai) Co.	N/A
Software and algorithms		
ChemDraw Professional 18.0	PerkinElmer	https://www.perkinelmerinformatics.com/products/research/chemdraw/
Maestro 11.5	Schrödinger	https://www.schrodinger.com/products/maestro
Desmond	Schrödinger	https://www.schrodinger.com/products/desmond
Glide	Schrödinger	https://www.schrodinger.com/products/glide

RESOURCE AVAILABILITY

Lead contact
Further information and requests for resources and reagents should be directed to and will be fulfilled by the lead contact, Prof. Hélder A. Santos (helder.santos@helsinki.fi).

Materials availability
All unique reagents generated in this study are listed in the key resources table and available from the lead contact with a completed Materials Transfer Agreement.

Data and code availability
The results presented in the study are available upon request from the lead contact.

EXPERIMENTAL MODEL AND SUBJECT DETAILS

MDA-MB-231 and HOS-MNNG cells were cultured in RPMI 1640 medium, NIH 3T3 fibroblasts and RAW264.7 macrophages were cultured in DMEM medium, both supplemented with 10% v/v of fetal bovine serum (FBS), 1% nonessential amino acids, 1% l-glutamine, penicillin (100 IU mL^{-1}), and streptomycin (100 mg mL^{-1}). Animal model in this study is BALB/c nude mice bearing HOS-MNNG tumors. Male BALB/c mice (20 ± 2g) were fed at the condition of 25°C and 55% of humidity and approved by the Institutional Animal Care and Use Committee of Ruijin Hospital. All animal experiments were performed in compliance with guidelines.

METHOD DETAILS

Synthesize of β-CD-BCN
The synthesize of β-CD-BCN was following previous reports (Jiang et al., 2014; Toomari et al., 2015). β-CD-OTs (264 mg, 205 μmol), BCN-amine (100 mg, 308 μmol) and Et3N (60 mg, 600 μmol) were dissolved in dry DMF and stirring under nitrogen flow. The mixture was heated to 70°C for 24 h. Then the solvent was removed under vacuum and acetone was added to get precipitation. The precipitation (200 mg) was collected and used for next step without further purification. The precipitation was confirmed to be β-CD-BCN under the characterization of Maldi-TOF. Calc. ($C_{59}H_{96}N_2O_{38}$): m/z = 1440.56, found: [M+H]$^+$ = 1441.32.

Synthesize of peptides
Peptide TCEVTELTREGETIIELK and GGGGYIGSR were synthesized on an automatic CEM peptide synthesizer on a scale of 250 μmol. Fmoc chemistry was applied for this synthesis and Sieber amide resin with a loading of 0.69 mmol g^{-1} was used. Amino acid couplings were performed with 4 eq. of the appropriate amino acid, 4 eq. of the activator HCTU and 8 eq. of the base DIPEA. Fmoc deprotection was performed with piperidine:DMF (4:6 v/v). After that N_3-PEG$_4$-COOH was coupled to the peptide on the resin using 4 eq. of DIPEA and 3 eq. of HOBT in DMF overnight. Peptides were cleaved from the resin by shaking the resin with a mixture of TFA/TIS/H2O (95:2.5:2.5 v/v) for 1.5 hour. The cleavage mixture was precipitated in cold diethyl ether. Precipitate was collected and the crude product was purified by HPLC. The pure peptides were measured and confirmed using LCMS. Peptide 1: Calc. ($C_{44}H_{73}N_{16}O_{16}$): m/z = 1081.54, found: [M+H]$^+$ = 1081.88, [M+2H]$^{2+}$ = 541.36; Peptide 2: Calc. ($C_{97}H_{169}N_{26}O_{37}S^+$): m/z = 2322.19, found: [M+2H]$^{2+}$ = 1162.76, [M+3H]$^{3+}$ = 774.3 and [M+4H]$^{4+}$ = 581.73.

Synthesize of β-CD-Self-peptides

The copper-free click reaction was achieved by mixing obtained peptide 2 (1 eq., 25 mg) and β-CD-BCN (1 eq., 15 mg) in water and stirred overnight at 40°C. The solvent was evaporated on rotavapor. The obtained compounds were purified by HPLC using H_2O/ACN (gradient: 90%–10%). The peak of β-CD-peptides 2 appears at around 30% of H_2O/ACN. The solution in collected peak solution was removed by freeze-drier to obtain white powder (~5 mg). The purity of β-CD-peptides 2 was proved by HPLC trace and the molecular mass was measured using Maldi-TOF. Calc. ($C_{156}H_{265}N_{28}O_{75}S^+$): m/z = 3765.02, found: $[m+H]^+$ = 3766.21.

^{1}H NMR spectra

^{1}H NMR spectra were measured on a Bruker AV-400MHz spectrometer. Chemical shifts were recorded in ppm. Tetramethylsilane (TMS) is used as an internal standard. Coupling constants are given in Hz.

MALDI-TOF mass spectra

MALDI-TOF mass spectra were acquired using an Applied Biosystems Voyager System 6069 MALDI-TOF mass spectrometer. α-Cyano-4-hydroxycinnamic acid (CHCA) was used as matrix in all cases. Sample concentrations were ~0.3 mg ml^{-1}.

LCMS analysis

LCMS analysis was performed on a Jasco HPLC-system coupled to a Perkin Elmer Sciex API 165 mass spectrometer.

CD spectra

CD spectra were measured using a Jasco J-815 spectropolarimeter. The observed ellipticity is given in milli-degrees, the conversion to the mean residue molar ellipticity is performed by the following Equation 1:

$$[\Theta] = \frac{\Theta_{obs}}{lC_M N},$$

(Equation 1)

where, Θ_{obs} is the observed ellipiticity, CM is the molar total peptide concentration, l is the path length of the cuvette in cm, and N is the number of amino acids per peptide (Zheng et al., 2013). Spectra were obtained at a sample concentration of 25 μM of peptide in water in a 0.1 cm quartz cuvette. All measurements were made at room temperature. Data was collected at 0.2 nm intervals, at a scanning speed of 20 nm min^{-1} and a 1 nm and width. Each spectrum was the average of 5 scans.

HPLC purifications of peptides

The HPLC was performed using a Shimadzu HPLC setup equipped with two LC-8A series pumps coupled to a Shimadzu ELSD-LT II detection system. Separation (Vydac 214 MS C4 column, 5 μm, 100 × 4.6 mm, flow rate: 15 mL min^{-1}), in all instances, was carried out over a linear gradient of 10%–90% B over 20 min with an initial 5 min hold at 10% B. HPLC buffers: A– H_2O (0.1% TFA) and B – ACN with 0.1% trifluoroacetic acid.

Peptide docking

The necessary part of peptide with 18 amino acids structure, was sketched through Maestro. The peptide complexes with hSIRPα were obtained via computational docking. Structural flexibility of the peptide was considered by sampling of 100 representative configurations from a 100 ns long MD trajectory using Desmond (Gianti and Zauhar, 2015). Binding of the peptide to the hSIRPα was evaluated using the docking suite Glide, the option of protocol designed specifically for peptides was ticked given its improved performance (Friesner et al., 2004; Tubert-Brohman et al., 2013). The known structure of hSIRPα with cell-surface protein CD47 complex (PDB: 2JJS) was split such that hSIRPα itself as proposed receptor of peptides, while the amino acids of CD47 at the interface plus extended 20 Å away served as the grid definer of peptides, using the "Generate grid suitable for peptide docking" option. The manual post-docking analysis elected top three reasonable binding poses of peptide, taking the docking score into account as well to determine the most likely binding poses of the polypeptide.

Preparation of UnTHCPSi NPs

The preparation of UnTHCPSi NPs was done via electrochemical anodization, as described in detail elsewhere (Bimbo et al., 2010).

Fabrication of the multistage signal interactive system

The UnTHCPSi NPs were treated with N-hydroxysuccinimide (NHS) and 1-ethyl-3-(3-(dimethylamino)propyl)-carbodiimide (EDC). Briefly, 10 mg of UnTHCPSi NPs was activated by 100 μL of EDC for 30 min and then reacted with 20 mg of NHS in 10 mL of anhydrous dimethylformamide (DMF) for 24 h. The obtained NPs were harvested by centrifugation (Sorvall RC 5B plus, Thermo Fisher Scientific, USA) at 13000 g for 5 min, then washed three times with anhydrous DMF. The obtained NPs was then dispersed into 10 mL of DMF with 100 mg of PEI dissolved beforehand. After 12 h stirring, the obtained UnTHCPSi-PEI NPs were harvested by the aforementioned procedures. 10 mg of UnTHCPSi-PEI NPs was suspended in 10 mL of anhydrous DMF, then 200 μg of BCN-PEG$_3$-NHS ester was added into the suspension. After 24 h stirring, the obtained UnTHCPSi-PEI-BCN NPs were harvested by the aforementioned procedures. Then 5 mg of the synthesized N$_3$-PEG$_4$-G$_4$YIGSR peptide was mixed with 10 mg of UnTHCPSi-PEI-BCN NPs in 10 mL of phosphate

buffer saline (PBS, pH 7.4, 0.01 M). After 24 h stirring, the NPs were harvested by centrifugation at 13000 g for 5 min, and washed by PBS (pH 7.4, 0.01 M) three times. The obtained UnTHCPSi-PEI-YIGSR NPs were stocked in 75% ethanol.

The UnTHCPSi-PEI-YIGSR-$^{\beta\text{-CD}}$Self-peptide NPs (^{Rev}SeMicNPs) were prepared just before use. 10 mg of the UnTHCPSi-PEI-YIGSR NPs were centrifuged and then dispersed into PBS (pH 7.4, 0.01 M), the $^{\beta\text{-CD}}$Self-peptide was added and then stirred 2 h. The mass ratio of the $^{\beta\text{-CD}}$Self-peptide to NPs was 1:2. Then the NPs was harvested by aforementioned method.

Characterization of the NPs

The hydrodynamic size (z-average), polydispersity index (PdI) and zeta-potential (ζ-potential) distribution of the NPs was measured by Zetasizer Nano ZS (Malvern Instruments Ltd.). The relevant data was recorded as the average of three measurements.

The structure of the fabricated NPs was characterized by transmission electron microscope (TEM) under an acceleration voltage of 120 kV. The NPs samples were prepared by depositing them onto carbon-coated copper grids (300 mesh; Electron Microscopy Sciences, USA) and contrasting with 2% uranyl acetate solution. The NPs coated grids were dried at room temperature before the TEM imaging.

Protein adsorption of the NPs

The NPs were incubated with 10% of human serum at pH 7.4, with the final concentration of NPs at 1 mg mL^{-1}. After incubation at 37°C for 2 h, 200 μL of each sample were centrifuged at 13000 g for 5 min to precipitate the protein adsorbed NPs. The protein concentration of supernatant was determined using UV-Vis spectroscopy (UV-1600 PB spectrophotometer, VWR) by measuring the maximal absorbance at 280 nm wavelength. Then, the adsorbed proteins on the NPs were calculated against a standard calibration curve of the proteins.

Drug loading degree

The loading degree of 17-AAG was tested by an immersion method. 10 mg of the prepared NPs were suspended in 1 mL of DMF in which 25 mg 17-AAG was dissolved, and then stirred for 2 h. The supernatant then was obtained after centrifugation, and the concentration of 17-AAG was determined by HPLC. For HPLC, the column used for 17-AAG detection was C18 (4.6 × 100 × 3 mm, Gemini-Nx plus C18, Phenomenex, USA), and the mobile phase used consisted of 0.2% of trifluoroacetic acid (pH 2) and ACN (40:60, v/v) with the flow rate of 1.0 mL min^{-1}. The temperature of the column and wavelength used for drug detection were 25°C and 254 nm, respectively. The injected volume of the drug solution was 20 μL.

Helical content detecting

Helical content was determined using Equation 2:

$$rh = \frac{[\theta]222}{-40 * 10^3 \deg cm^2\, dmol^{-1}\left(1 - \frac{4.6}{N}\right)} \times 100,$$ (Equation 2)

where, rh is the helical fraction, $[\theta]222$ is the ellipticity at 222 nm and N is the number of peptide bonds (Rabe et al., 2015).

Cell culturing

The MDA-MB-231 breast cancer cells, NIH 3T3 fibroblasts, HOS-MNNG cells and RAW264.7 macrophages were cultured in 75 cm^2 flasks (Corning Inc. Life Sciences, USA) in a standard BB 16 gas incubator (Heraeus Instruments GmbH, Germany) set at 95% humidity, 5% CO$_2$, and 37°C. MDA-MB-231 and HOS-MNNG cells were cultured in standard RPMI 1640 medium, NIH 3T3 fibroblasts and RAW264.7 macrophages were cultured in DMEM medium, both supplemented with 10% v/v of fetal bovine serum (FBS), 1% nonessential amino acids, 1% l-glutamine, penicillin (100 IU mL^{-1}), and streptomycin (100 mg mL^{-1}) (all from HyClone, USA). Cells' subculturing was conducted at 80% confluency, harvested prior to cell passaging and each experiment with trypsin−PBS−ethylenediaminetetraacetic acid.

Western-blotting

For protein extraction, cells at rest were washed with ice-cold PBS containing 100 μM Na$_3$VO$_4$ (Sigma, China), PMSF and lysed with ice-cold lysis buffer at 4°C for 15 min. Then supernatants were collected after centrifugation at 16000 g for 15 min. Concentration of protein within lysate was determined using Folin-Lowry assay method. The extracts proteins were separated on a 7.5% SDS-PAGE for electrophoresis. Then the cell lysate was transferred onto polyvinylidene fluoride membranes, and then blocked overnight at 4°C with 2% BSA in TBST (12.5 mM Tris/HCl, pH 7.6, 137 mM NaCl, 0.1% Tween 20). After washing with TBST, blots were incubated for 2 h at room temperature with rabbit polyclonal anti-SIRPα (Thermofisher Scientific, China) and then HRP was labeled as secondary antibody. Membranes were washed extensively and then detected using Enhanced Chemiluminescence Plus Western-blotting detection system (Amersham, USA).

In vitro cytotoxicity

To evaluate the biosafety of the NPs, the viability of the NIH 3T3 fibroblast, MDA-MB-231 and HOS-MNNG cells were assessed by measuring their ATP activity after exposure to the NPs. Hundred microliters of the cell suspensions in cell media at a concentration of

2×10^5 cells per mL were seeded in 96-well plates and allowed to attach overnight. After the removal of the cell media, the wells were washed twice with HBSS–HEPES (4-(2-hydroxyethyl)-1-piperazineethanesulfonic acid) buffer (pH 7.4), and then 100 μL of the tested NPs at the relevant concentrations was added. After incubation, the reagent assay (100 μL; CellTiter-Glo Luminescent Cell Viability Assay, Promega, USA) was added to each well to assess the ATP activity. The luminescence was measured using a Varioskan Flash (Thermo Fisher Scientific Inc., USA). Positive (1% Triton X-100) and negative (HBSS–HEPES buffer, pH 7.4) controls were also used and treated similarly as described above. At least three independent measurements were conducted for each experiment.

Confocal fluorescence microscopy imaging

For the test, NIH 3T3 fibroblasts, MDA-MB-231 cells, HOS-MNNG and RAW264.7 macrophage cells were seeded in 8-chamber slides (Nunc Lab-Tek II Chamber Slide System, Thermo Scientific, Inc., USA). For cell seeding, 200 μL of the cells suspension (2.5×10^4 cells mL^{-1}) was added to each chamber. After incubation for 24 h, the cells were washed twice with HBSS–HEPES buffer (pH 7.4). 200 μL of fluorescein isothiocyanate (FITC)– labeled NPs (10 μg mL^{-1}) was added to each chamber, and then the samples were incubated for 6 h. After that, the cells were washed with HBSS–HEPES buffer to remove non-interacting NPs. The cell membrane was stained with CellMask Deep Red (Life Technologies, USA) by incubating the cells at 37°C for 3 min. Next, the cells were washed twice with the HBSS–HEPES buffer and fixed with 2.5% of glutaraldehyde at room temperature for 20 min. Finally, the glutaraldehyde was washed away, and the cells were stored with 200 μL of HBSS–HEPES buffer (pH 7.4). The cells were observed under a confocal fluorescence microscope (Leica inverted SP5 II HCS A) using Ar (488 nm), HeNe (590 nm), and HeNe (633 nm) lasers. The images were analyzed using ImageJ 1.47v (National Institute of Health, USA).

Cell uptake flow cytometry analysis

MDA-MB-231, 3T3 fibroblasts, and RAW264.7 macrophage cells were seeded in 6-well plates (Corn ing Inc., Life Sciences, USA). For cell seeding, 2.5 mL of the cells suspension (2×10^5 cells per mL) were added to each well. The cell culturing process was based on the aforementioned method. After that, 1.5 mL of NPs in HBSS–HEPES buffer with the concentration of 10 μg mL^{-1} were added to each well and then the samples were incubated for relevant time. After removing the NPs suspensions and washing twice with HBSS–HEPES buffer, the cells were harvested and treated with trypan blue to quench the fluorescence of NPs adhered on cell surface. Flow cytometry was performed with a LSR II flow cytometer (BD Biosciences, USA) with a laser excitation wavelength of 488 nm using a FACSDiva software. Ten thousand events were obtained for each sample. Relevant data were analyzed and plotted using FlowJo software (Tree Star Inc., USA). At least three independent measurements were conducted for each experiment.

Cell growth inhibition

The cell growth inhibition performance of the developed NPs was also monitored by measuring the antiproliferation effect of the free drug and drug-loaded NPs using the same method explained above for the cellular toxicity studies. At least three independent measurements were conducted for each experiment.

Biodistribution investigation

The HOS-MNNG cells (2×10^6 cells per each mouse) were subcutaneously injected into the flanks of male BALB/c mice (20 ± 2g) to construct the tumor-bearing mice. Then, the mice were injected intravenously with different therapeutics at the doses of 10 mg kg^{-1} of NPs, which were labeled with Cy 7.5. Tissues, including heart, liver, spleen, lung, kidney, and tumor were extracted from the mice 72 h post-injection for *ex vivo* near infrared fluorescence (NIRF) imaging.

In vivo NIRF imaging

The prepared therapeutics were injected intravenously into the BALB/c nude mice bearing HOS-MNNG tumors at a dose of 10 mg kg^{-1} of NPs. Then, the mice were imaged using IVIS Lumina II with the excitation wavelength of 780 nm at 3, 6, 12, 24, 48, 72 h post-injection. The average NIRF intensity at the tumor was calculated to describe the signals at different time points.

Ex vivo histological staining

The mice under 35-day treatment by the various formulations, including PBS, free AS1411, free 17-AAG, control-NPs, RevSemicNPs, and RevSemicNPs+Ad were dissected. Various tissues, including heart, liver, spleen, lung, kidney, and tumor were fixed in a 4% of formaldehyde solution for 24 h at room temperature. The various tissues were frozen and sectioned at the thickness of 10 μm. H&E staining (BBC Biochemical, Mount Vernon, WA) was performed and observed using an IX73 bright-field microscope (Olympus).

QUANTIFICATION AND STATISTICAL ANALYSIS

Quantitative data collected over multiple, independent experiments are presented as mean ± standard deviation (SD). At least three independent experiments (n = 3) were performed to obtain the described results. Statistical significance of the data was analyzed by a one-way analysis of variance (ANOVA) with Bonferroni post hoc test (GraphPad Prism, GraphPad software Inc., CA, USA). The significance level was set at probabilities of $^*p < 0.05$, $^{**}p < 0.01$, and $^{***}p < 0.001$.